

**Seasonal propagation of sea level along the
equator in the Atlantic**

by

Lucia Bunge and Allan J. Clarke

Department of Oceanography

Florida State University

Tallahassee, FL 32306-4320

Email: bunge@ocean.fsu.edu ;

clarke@ocean.fsu.edu

Revision

Journal of Physical Oceanography

Abstract

In the equatorial Atlantic the sea surface height anomaly (SSH) field is dominated by an annual signal propagating eastward. This signal has been previously interpreted in terms of propagating waves. In this paper we argue that this propagating signal is not a free equatorial Kelvin wave because the phase velocity observed is too small compared to 1st, 2nd or 3rd baroclinic mode Kelvin waves and is not the result of an equatorial forced wave because the zonal wind stress does not show a similar propagation. Rather, we suggest that the eastward propagation in SSH is due to the sum of two independent modes of variability, one mainly driven by the wind stress curl off the equator, and the other driven by the zonal wind stress along the equator. These two modes are uncorrelated in time and space and therefore can be conveniently separated by an empirical orthogonal function analysis of the equatorial Atlantic sea surface height. The first mode explains 74% of the variance, is one-signed in longitude, and is interpreted as the variability of the warm water volume above the thermocline. The second mode explains 24% of the variance, consists of an east-west tilt along the equator, and is driven by variations of the zonal equatorial wind stress.

(209 words)

Introduction

The seasonal cycle is the largest atmosphere-ocean signal in the equatorial Atlantic and is commonly described in terms of the sea surface temperature (SST) and zonal wind fields. When the Inter Tropical Convergence Zone (ITCZ) is close to the equator (January through May), weak and variable winds prevail and the SSTs in the eastern tropical Atlantic reach their maximum values. As the ITCZ migrates northward in boreal summer, the south-easterly trade winds pick up and the winds along the equator intensify, displacing eastern surface waters to the west. The resulting zonal pressure gradient in the ocean and associated uplifting of the thermocline leads to the lowering of SST in the eastern region (e.g., Weingartner and Weisberg 1991; Li and Philander 1997).

From the above description of the SST and zonal wind annual cycle, one might expect that the main signal in the sea surface height (SSH) field at the equator could be represented by an east-west tilt: SSH in the east would then be negatively correlated to SSH in the west and, somewhere in between the east and the west, there would be a zone of low amplitude variability, representing the node of the tilt. This, however, is not the case; rather, the annual SSH signal in the equatorial Atlantic propagates eastward at a speed of about 0.4 m s^{-1} (Fig. 1a). Merle (1980) first established this result for the annual signal of the depth of the thermocline, a variable proportional to the SSH. He found that it propagated eastward with a phase speed of approximately 30 cm/s, nearly an order of magnitude smaller than the first baroclinic mode Kelvin speed. Recently, the SSH annual signal was interpreted as the result of a cycle of consecutive Kelvin and Rossby waves of mainly baroclinic modes 2 and 3 (Schouten et al. 2005).

In this paper, we argue that the annual eastward propagating signal in SSH at the equator is actually not the result of propagating waves, but rather the superposition of two independent modes of variability. The idea of two independent modes comes from studies in the equatorial Pacific where interannual fluctuations of the thermocline depth also propagate eastward (Li 1997). In the Pacific, at interannual time scales, the depth of the thermocline varies as two different dynamical modes (e.g., Meinen and McPhaden 2000). The first mode is zonally asymmetric and represents the tilt of the thermocline. It is driven by the zonal wind stress and is approximately in phase with it. The second mode, not in equilibrium with the equatorial winds, corresponds to a zonal-mean depth anomaly which can be interpreted as the warm water volume accumulated above the thermocline. This zonally symmetric mode in the Pacific is in fact driven by meridional variations in the wind stress curl (Li 1997; Clarke et al. 2007). It was Li (1997) who surmised that it is the combination of the two modes, i.e., the zonally symmetric and the zonally asymmetric, that causes an apparent eastward propagation of the thermocline depth interannual signal in the Pacific.

In the Atlantic, the zonally asymmetrical thermocline mode associated with the tilt of the thermocline is well documented (e.g., Katz 1977; Katz et al. 1986; Provost et al. 2006). Using satellite data, Provost et al. (2006) showed that variations in the zonal wind stress are closely related to the zonal sea surface slope anomaly at both annual and interannual time scales. For the zonally symmetric heat content mode, we expect that it must exist since the wind stress curl that drives it plays a major role in Atlantic equatorial ocean dynamics (e.g., Arhan et al. 2006). This paper documents the existence of this zonally symmetric mode and shows that it is in fact the dominant mode of Atlantic

equatorial thermodynamics and SSH variability. We will also show that the sum of this mode and the zonally asymmetric tilt mode explains the observed eastward SSH and thermocline depth propagation. In all the analysis to follow we have removed the time mean of all variables so only the time dependent part is being considered.

The paper is organized as follows: In section 2 we present the results of the SSH- EOF analysis, documenting the dominance of the zonally symmetric mode and discussing how this mode is forced. Section 3 analyzes why the propagation observed is not due to equatorial waves and summarizes the results.

2. The two equatorial Atlantic SSH modes of variability

To separate the principal modes of variability along the equatorial Atlantic, an EOF analysis was performed on equatorial SSH time series that are a function only of time and longitude (from 42°W to 10°W). These time series were constructed by meridionally averaging the data between 2°S and 2°N (Fig. 2). The SSH data were obtained from the AVISO gridded satellite products, combining all accessible altimetry satellites (TOPEX/Poseidon, Jason-1, Envisat, and ERS-1/2) for the years between 1992 and 2007. The data are monthly, have a spatial resolution of 1/3° and are available at <http://www.aviso.oceanobs.com>. The choices for the eastern and western longitudes are based on several factors. The region west of 42°W is dominated by a very energetic mesoscale field related to the retroflexion of the North Brazil Current (Provost et al. 2004). Variability in this region has high amplitudes at intraseasonal time scales which are not relevant for our purposes. East of 10°W, the local variability is specific to the Gulf of Guinea because the prevailing winds are greatly affected by the African continent

(Li and Philander 1997). Finally, the latitudinal extent of the box was constrained by the presence of the South American coast (Fig. 2).

The EOF analysis shows two principal modes of variability (Fig. 3) which together explain 98% of the variance of the SSH in the region. The first mode, explaining 74% of the variability, does not change sign with longitude and is strongest in the western part of the box. The second mode explains 24% of the variance and is an east-west tilting mode (zonally asymmetric), with a node at around 28°W. The 20°C isotherm depth, available from the Pilot Research Moored Array in the Atlantic (PIRATA) research program, is highly positively correlated with the SSH (see Fig. 4). The correlation is ≥ 0.9 ; the true correlation is greater than zero with 95% probability when $r \geq r_{crit} = 0.57$. Here and elsewhere in this paper r_{crit} is based on Ebisuzaki (1997). Based on this high correlation, as in the Pacific, these modes of variability should also exist for the equatorial Atlantic 20°C isotherm depth. The first Atlantic equatorial mode may thus be regarded as a nearly zonally symmetric increase and decrease in the 20°C isotherm depth, i.e., as variations in the warm water volume (WWV) above the 20°C isotherm.

The tilt and WWV equatorial modes in the Pacific and Atlantic differ in two ways; in the Atlantic, the low-frequency variability is approximately annual and the WWV mode is much larger than the tilt mode. In contrast, in the Pacific, the low-frequency variability is interannual and the relative importance of the modes is more evenly shared. In other respects, the two dominant Atlantic and Pacific EOF modes are similar. In both the Pacific (Kessler 1990; Li and Clarke 1994; Meinen and McPhaden 2000; Clarke et al. 2007) and Atlantic (Katz et al. 1986; Provost et al. 2006), the tilt mode

is in phase and proportional to the zonal equatorial wind stress, in accordance with an approximate balance between the zonal wind stress forcing τ^x and the zonal pressure gradient p_x integrated from the depth h of the 20°C isotherm to the surface:

$$\int_{-h}^0 p_x dz = \tau^x. \quad (2.1)$$

In the equatorial Pacific (Meinen and McPhaden 2000; Clarke et al. 2007), the tilt principal component $\phi_{\text{tilt}}(t)$ and the WWV principal component $\phi_{\text{WWV}}(t)$ were shown to be approximately in quadrature, i.e.,

$$\alpha \frac{\partial \phi_{\text{WWV}}}{\partial t} \approx \phi_{\text{tilt}}, \quad (2.2)$$

for some positive constant α . In the Atlantic we find a similar result, the correlation coefficient between the time series $\frac{\partial \phi_{\text{WWV}}}{\partial t}$ and ϕ_{tilt} at zero lag being $r = 0.67$ ($r_{\text{crit}}(95\%) = 0.47$) and the regression coefficient $\alpha = 1.67$ months (Fig. 5). As noted by a reviewer, even though the time series in (2.2) are on average in phase, there are small lags of both signs depending on the year. A possible explanation of this is that the difference in zonal transport between the eastern and western ends of the box is not negligible. For example, observations and model results (Katz et al. 1981; Arhan et al. 2006) have shown that the maximum transport of the equatorial undercurrent (EUC) in the western part of the basin occurs during the northern hemisphere spring. This transport would increase the WWV at a time when the meridional transports due to the wind curl are causing water to leave the box. The magnitude of the EUC spring transport

maximum varies greatly from year to year (Arhan et al. 2006) and this may contribute to small phase lags of the WWV mode with respect to the tilt mode.

Why should we expect the WWV and tilt modes to be in quadrature, i.e., why should (2.2) hold? The physics of the WWV mode has been discussed in detail for the Pacific by Clarke et al. (2007). The main idea can be qualitatively illustrated by considering the simple case of a two layer ocean model with upper layer depth h . If we integrate the upper layer continuity equation

$$h_t + (hu)_x + (hv)_y = 0 \quad (2.3)$$

over the equatorial box of Fig. 2, and assume that the horizontal divergence is mainly meridional, then, by the divergence theorem, (2.3) becomes

$$\frac{\partial}{\partial t} \int_A h dA = \int_{y=y_S} h v dx - \int_{y=y_N} h v dx . \quad (2.4)$$

In other words, the $\frac{\partial}{\partial t}(\text{WWV})$ [the left hand side of (2.4)] is equal to the northward transport into the box along its southern edge $y = y_S$ plus the southward transport into the box along its northern edge $y = y_N$. According to Sverdrup balance, the net meridional transport is largely due to the wind stress curl. From (2.4), this would mean that $\frac{\partial}{\partial t}(\text{WWV})$ would be proportional to the zonally integrated wind stress curl along the southern edge of the box minus the zonally integrated wind stress curl along the northern edge of the box. We will label this curl difference Δcurl .

Since this Δ curl drives $\frac{\partial}{\partial t}(\text{WWV})$ and the zonal wind stress drives the sea level tilt (see (2.1)), the in quadrature relationship (2.2) will hold if Δ curl varies in time like the zonal wind stress. We tested this by using the Florida State University (FSU) wind stress data, downloaded from <http://www.coaps.fsu.edu/scatterometry/>, to compute the box averaged eastward wind stress τ^x and Δ curl. The FSU data consist of QuikSCAT scatterometer wind speed and wind pseudo stresses for the years 1999 to 2005. The gridded product is monthly and has a spatial resolution of $1/2^\circ$. To calculate the wind stress, pseudo stresses were multiplied by an average density of 1.16 kg/m^3 , estimated using the PIRATA mooring array, and a drag coefficient which was calculated using the formulae of Large et al. (1994).

Figure 6 shows that the box-averaged westward wind stress is in phase and proportional to Δ curl. This is consistent with the observations in Fig. 3 and the qualitative physics we have proposed. For example, since S is positive (see Fig. 3), when the $\text{WWV} = \phi_{\text{WWV}} S$ is increasing in time, $\frac{\partial \phi_{\text{WWV}}}{\partial t} > 0$ and so, by (2.2) $\phi_{\text{tilt}} > 0$. From Fig. 3, when ϕ_{tilt} is positive, the sea level tilt component $\phi_{\text{tilt}} T$ tilts up toward the west. But Sverdrup physics says that increasing WWV in the box corresponds to net flow into the box and therefore to positive Δ curl. Since Δ curl is proportional to westward wind stress (Fig. 6), and westward wind stress is proportional to a sea level tilt upward toward the west, we see qualitatively how the observed in quadrature relationship of Fig. 3 may arise.

While (2.2) and the observed phase relationship between WWV and tilt is consistent with an argument based on Sverdrup dynamics, as mentioned before and as shown by Clarke et al. (2007) in the Pacific, quantitatively, other factors enter the dynamics. For example, the horizontal convergence is not just meridional and the wind stress curl not only generates meridional transport (Sverdrup balance), but also generates $\partial h/\partial t$ locally. However, these factors, on average, do not qualitatively alter (2.2).

3. Summary and discussion

The results presented here disagree with previous analyses trying to explain the SSH propagation along the equator in terms of waves. Specifically, our results disagree with the results of Schouten et al. (2005) who interpreted the eastward propagating signal in the Atlantic at the equator as the propagation of Kelvin waves. We do not think the eastward propagation observed in SSH is due to freely propagating waves for three main reasons. First and most important, the phase speed of the propagation is too slow compared to that of the first, second, or third baroclinic modes; even the phase speed of third baroclinic mode Kelvin wave is 2 to 3 times larger than the propagation observed (110 cm/s vs 30-50 cm/s). Second, the propagating signal has large amplitude in the west because it is there that the changes in the wind stress curl are strongest. A Kelvin wave propagating across the Atlantic cannot explain why the amplitude of the signal is strongest in the west. Third, equivalent observations of the 20°C isotherm in the Pacific have also been shown to be the result of two modes with similar characteristics of the ones found in the Atlantic (e.g., Li 1997; Meinen and McPhaden 2000; Clarke et al. 2007).

We do not think the eastward propagation observed in SSH is due to a forced wave either. The theory of wind-forced equatorial waves (e.g., Gill and Clarke, 1974) indicates that if the observed SSH propagation were due to a forced wave, then the observed zonal equatorial wind stress should propagate eastward at the same speed as the observed SSH. But the zonal equatorial seasonal wind stress does not do this (Fig. 7).

The annual fluctuation of SSH and 20°C isotherm depth in the equatorial Atlantic can be explained, instead, as the sum of two independent dynamical modes: The first mode can be regarded as the variations in the warm water volume above the 20°C isotherm and the second mode represents a tilt in the thermocline. Because these two modes are uncorrelated in time and space, they can be conveniently separated by empirical orthogonal functions. The principal components of both modes are in quadrature. The in quadrature relationship, the dominance of the one signed WWV mode and the linear slope of the tilt mode gives rise to the apparent propagation of the annual signal as observed in SSH time-longitude diagrams.

Acknowledgments. We are grateful for funding from the National Science Foundation (Grants OCE-0220563 and ATM-0623402). The altimeter products were produced by SSALTO/ DUACS and distributed by AVISO, with support from CNES. The buoy data were obtained from the PIRATA Project and the gridded QuikSCAT data were produced by COAPS/FSU through support by the NASA Ocean Vector Winds Science Team. We warmly thank Mark A. Bourassa for his help in understanding different wind products.

References

- Arhan, M., A. M. Treguier, B. Bourlès and S. Michel, 2006: Diagnosing the annual cycle of the Equatorial Undercurrent in the Atlantic Ocean from a General Circulation Model. *J. Phys. Oceanogr.*, **36**, 1502-1522.
- Clarke, A. J., S. Van Gorder and G. Colantuono, 2007: Wind stress curl and the ENSO discharge/recharge in the equatorial Pacific. *J. Phys. Oceanogr.*, **37**, 1077-1091.
- Ebisuzaki, W., 1997: A method to estimate the statistical significance of a correlation when the data are serially correlated. *J. Climate*, **10**, 2147-2153.
- Gill, A. E., and A. J. Clarke, 1974: Wind-induced upwelling, coastal currents and sea-level changes. *Deep-Sea Res.*, **21**, 325-345.
- Katz, E. J., 1977: Zonal pressure gradient along the equatorial Atlantic. *J. Mar. Res.*, **35**, 293-307.
- Katz, E. J., P. Hisard, J. M. Verstraete and S. L. Garzoli, 1986: Annual change of sea surface slope along the equator on the Atlantic Ocean in 1983 and 1984. *Nature*, **222**, 245-247.
- Katz E. J., R. L. Molinari, D. E. Cartwright, P. Hisard, H. U. Lass, and A. deMesquita, 1981: The seasonal transport of the Equatorial Undercurrent in the western Atlantic (during the Global Weather Experiment). *Oceanol. Acta*, **4**, 445-450.
- Kessler, W. S., 1990: Observations of long Rossby waves in the northern tropical Pacific. *J. Geophys. Res.*, **95**, 5183-5217.
- Large, W. G., J. C. McWilliams, and S. C. Doney, 1994: Oceanic vertical mixing: A review and a model with a vertical K-profile boundary layer parameterization. *Rev. Geophys.*, 363-403.

- Li, B. and A. J. Clarke, 1994: An examination of some ENSO mechanisms using interannual sea level at the eastern and western equatorial boundaries and the zonally averaged equatorial wind. *J. Phys. Oceanogr.*, **24**, 681-690.
- Li, T., 1997: Phase transition of the El Niño-Southern Oscillation: A stationary SST mode, *J. Atmos. Sci.*, **54**, 2872-2887.
- Li, T., and S. G. H. Philander, 1997: On the seasonal cycle of the equatorial Atlantic ocean. *J. Climate*, **10** (4), 813-817.
- McArdle, B. H., 1988: The structural relationship: Regression in biology. *Can. J. Zool.*, **66**, 2329-2339.
- Meinen, C. S., and M. J. McPhaden, 2000: Observations of warm water volume changes in the equatorial Pacific and their relationship to El Niño and La Niña. *J. Climate*, **13**, 3551-3559.
- Merle, J., 1980: Seasonal heat budget in the equatorial Atlantic Ocean. *J. Phys. Oceanogr.*, **10**, 464-469.
- Provost, C., S. Arnault, N. Chouaib, A. Kartavtseff, L. Bunge and E. Sultan, 2004: TOPEX/Poseidon and Jason equatorial sea surface slope anomaly in the Atlantic in 2002: Comparison with wind and current measurements at 23W. *Marine Geodesy*, **27**, 31-45.
- Provost, C., N. Chouaib, A. Spadone, L. Bunge, S. Arnault, and E. Sultan, 2006: Interannual variability of the zonal sea surface slope at the equator in the Atlantic in the 1990's. *J. Adv. Space Res.*, **37** (4), 823-831. doi:10.1016/j.asr.2005.06.018.
- Schouten, M. W., R. P. Matano, and T. P. Strub, 2005: A description of the seasonal cycle of the equatorial Atlantic from altimeter data. *Deep-Sea Res. I*, **52**, 477-493.
- Weingartner, T., and R. H. Weisberg, 1991: A description of the annual cycle in sea surface temperature and upper ocean heat in the equatorial Atlantic. *J. Phys. Oceanogr.*, **21** (1), 83-96.

Figure Captions

Figure 1: (a) Longitude-time diagram of the seasonal signal of SSH (in cm). The satellite data were averaged between 2°N and 2°S. The strongest signal is annual and depicts an apparent eastward propagation at a speed of about 0.4 m/s (heavy dashed line). (b) Same as in (a) but for the sum of the first two SSH-EOFs. This sum accounts for 98% of the variability and, like the unprocessed SSH, gives the visual impression of an annual eastward propagating signal.

Figure 2: Map of the tropical Atlantic showing the extent of the domain considered in this analysis. The box limits are 2°S and 2°N, and 42°W and 10°W. The solid triangles represent the position of two equatorial moorings from the PIRATA array at 35°W and 23°W. The 20°C isotherm depth from these moorings is described in section 2.

Figure 3: First (solid line) and second (dot-dash line) EOF (a) and principal components (b) of the equatorial SSH in the study domain (see Fig. 2). The principal component time series has been normalized to have variance = 0.5 so that (a) represents the amplitude of the SSH in cm. The first mode explains 74% of the variance and has the same sign for all longitudes. The second mode explains 24% of the variance and consists on an east-west tilt with a node at around 28°W. Consistent with ϕ_{ilt} leading ϕ_{Wwv} in (b), ϕ_{ilt} is proportional to a positive constant times $\partial\phi_{\text{Wwv}}/\partial t$ (see (2.2)). The tick marks on the time axis in (b) next to the years correspond to June 15th of a particular year.

Figure 4: Time series of PIRATA 20° C isotherm depth anomaly and satellite SSH at 23°W (a) and at 35°W (b). See Fig. 2 for the position of PIRATA moorings. The SSH has been multiplied by a regression coefficient of 307 (a) and 311 (b). This implies that a change in SSH of 1 cm is equivalent to a change of approximately 3 m in the 20°C isotherm depth. To estimate the regression coefficients, we used the ratio of standard deviations of the series because it is more accurate than the standard least squares regression coefficient when both time series have comparable noise to signal ratios (McArdle 1988). The tick marks on the time axis next to J, A, J, and O respectively correspond to January 15th, April 15th, July 15th and October 15th of a particular year. In each panel r is the correlation coefficient and r_c the 95% critical correlation coefficient.

Figure 5: The left hand side ($\alpha \frac{\partial \phi_{wvw}}{\partial t}$, dashed line) and the right hand side (ϕ_{ilt} , solid line) of equation (2.2). The correlation coefficient between series is $r = 0.67$ with $r_{crit}(95\%) = 0.47$ and $\alpha = 1.67$ months. The tick marks on the time axis next to the years correspond to June 15th of a particular year.

Figure 6: Seasonal variations of the wind stress curl difference Δ curl (solid line) and the westward wind stress (dashed line) for the box in Fig. 2. The curl difference, which is proportional to the net meridional Sverdrup transport entering the box, was calculated by integrating the wind stress curl along the southern edge of the box and subtracting the wind stress curl integrated along the northern edge. The time series in the plot have been normalized by their standard deviations.

Figure 7: Longitude-time diagram of the seasonal signal of the zonal wind stress (in $\text{Nm}^{-2} \times 1000$). The satellite data were averaged between 2°N and 2°S.

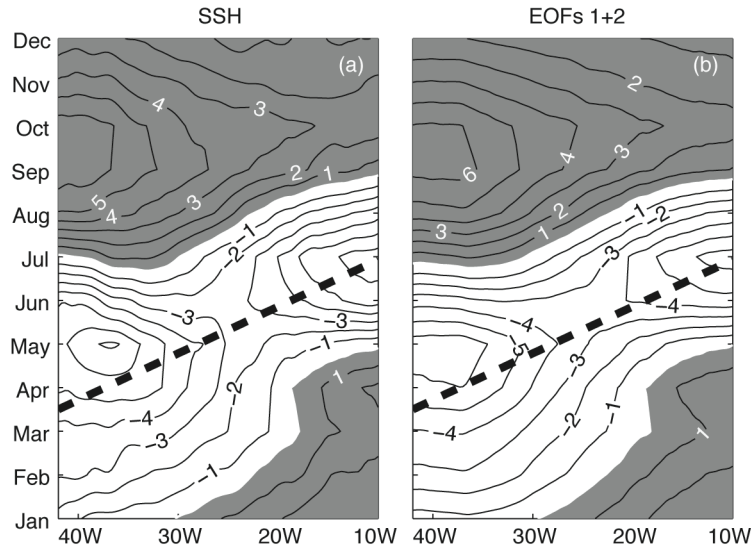


Figure 1: (a) Longitude-time diagram of the seasonal signal of SSH (in cm). The satellite data were averaged between 2°N and 2°S. The strongest signal is annual and has an apparent eastward propagation at a speed of about 0.4 m/s (heavy dashed line). (b) Same as in (a) but for the sum of the first two SSH-EOFs. This sum accounts for 98% of the variability and, like the unprocessed SSH, gives the visual impression of an annual eastward propagating signal.

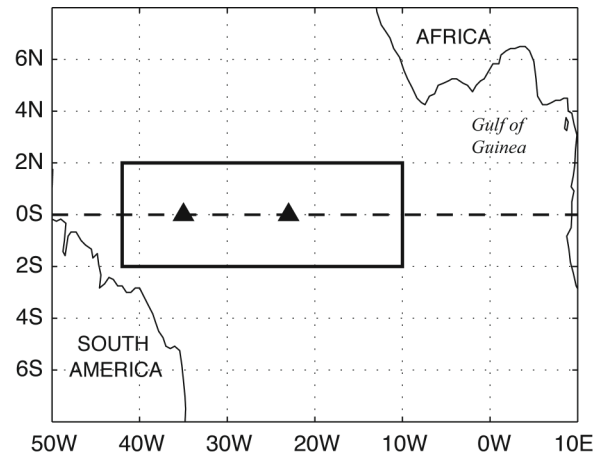


Figure 2: Map of the tropical Atlantic showing the extent of the domain considered in this analysis. The box limits are 2°S and 2°N, and 42°W and 10°W. The solid triangles represent the position of two equatorial moorings from the PIRATA array at 35°W and 23°W. The 20°C isotherm depth from these moorings is described in section 2.

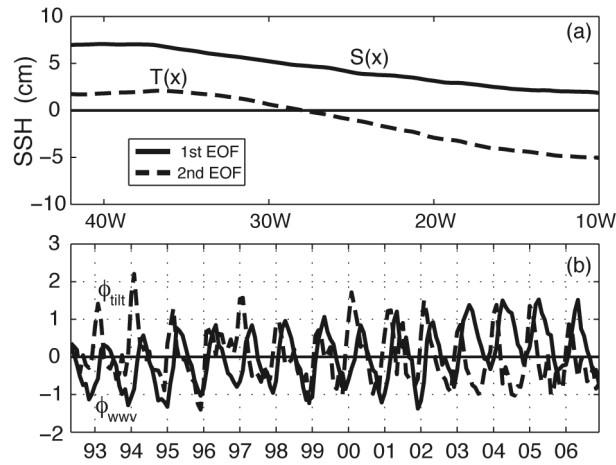


Figure 3: First (solid line) and second (dot-dash line) EOF (a) and principal components (b) of the equatorial SSH in the study domain (see Fig. 2). The principal component time series has been normalized to have variance = 0.5 so that (a) represents the amplitude of the SSH in cm. The first mode explains 74% of the variance and has the same sign for all longitudes. The second mode explains 24% of the variance and consists on an east-west tilt with a node at around 28°W. Consistent with ϕ_{tilt} leading ϕ_{wwv} in (b), ϕ_{tilt} is proportional to a positive constant times $\partial\phi_{\text{wwv}}/\partial t$ (see (2.2)). The tick marks on the time axis in (b) next to the years correspond to June 15th of a particular year.

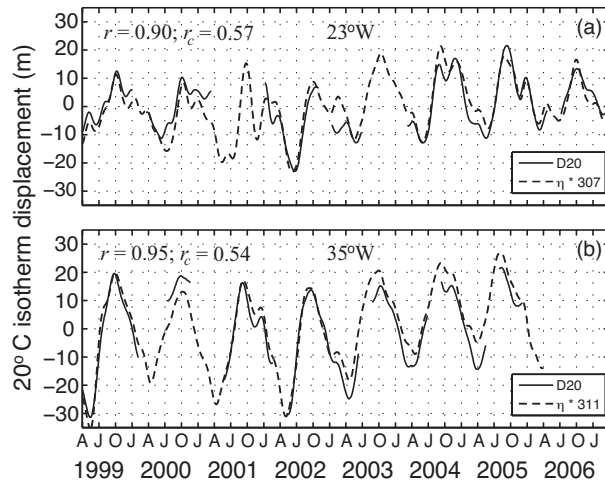


Figure 4: Time series of PIRATA 20° C isotherm depth anomaly and satellite SSH at 23°W (a) and at 35°W (b). See Fig. 2 for the position of PIRATA moorings. The SSH has been multiplied by a regression coefficient of 307 (a) and 311 (b). This implies that a change in SSH of 1 cm is equivalent to a change of approximately 3 m in the 20°C isotherm depth. To estimate the regression coefficients, we used the ratio of standard deviations of the series because it is more accurate than the standard least squares regression coefficient when both time series have comparable noise to signal ratios (McArdle 1988). The tick marks on the time axis next to J, A, J, and O respectively correspond to January 15th, April 15th, July 15th and October 15th of a particular year.

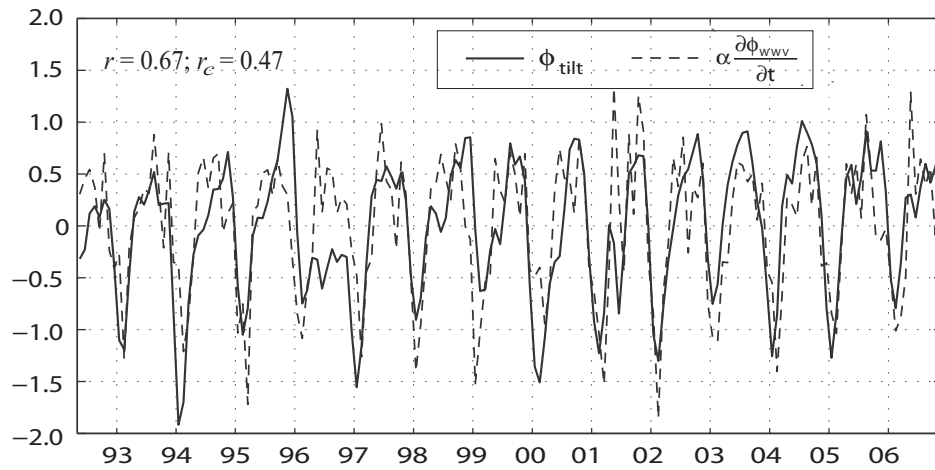


Figure 5: The left hand side ($\alpha \frac{\partial \phi_{wv}}{\partial t}$, dashed line) and the right hand side (ϕ_{tilt} , solid line) of equation (2.2). The correlation coefficient between series is $r = 0.67$ with $r_{crit}(95\%) = 0.47$ and $\alpha = 1.67$ months. The tick marks on the time axis next to the years correspond to June 15th of a particular year.

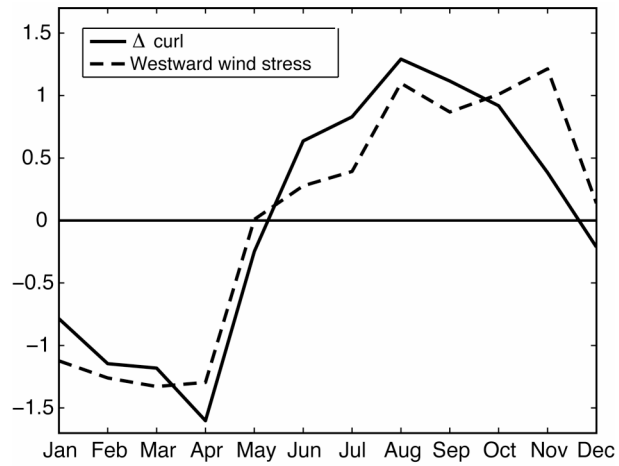


Figure 6: Seasonal variations of the wind stress curl difference Δ curl (solid line) and the westward wind stress (dashed line) for the box in Fig. 2. The curl difference, which is proportional to the net meridional Sverdrup transport entering the box, was calculated by integrating the wind stress curl along the southern edge of the box and subtracting the wind stress curl integrated along the northern edge. The time series in the plot have been normalized by their standard deviations.

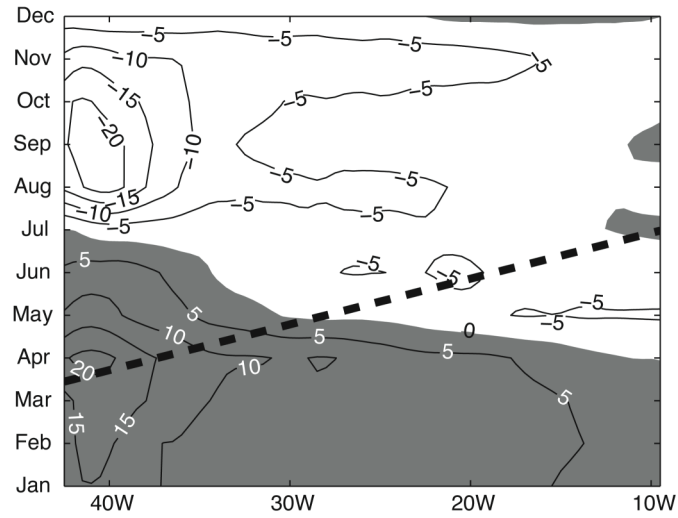


Figure 7: Longitude-time diagram of the seasonal signal of the zonal wind stress (in $\text{Nm}^2 \times 1000$). The satellite data were averaged between 2°N and 2°S . The heavy dashed line depicts an eastward propagation of 0.4 m/s seen in the SSH (see Fig.1).